

# Universal equivalent circuit model and verification of current source for triboelectric nanogenerator

Da Zhao<sup>a,b,1</sup>, Xin Yu<sup>a,1</sup>, Zhenjie Wang<sup>a</sup>, Jianlong Wang<sup>a,b</sup>, Xiang Li<sup>a</sup>, Zhong Lin Wang<sup>a,c,d,\*</sup>, Tinghai Cheng<sup>a,b,c,\*</sup>

<sup>a</sup> Beijing Institute of Nanoenergy and Nanosystems, Chinese Academy of Sciences, Beijing 101400, China

<sup>b</sup> School of Mechatronic Engineering, Changchun University of Technology, Changchun, Jilin 130012, China

<sup>c</sup> CUSTech Institute, Wenzhou, Zhejiang 325024, China

<sup>d</sup> School of Materials Science and Engineering, Georgia Institute of Technology, Atlanta, GA 30332-0245, USA

## ARTICLE INFO

### Keywords:

Triboelectric nanogenerator  
Current source  
Universal equivalent circuit model  
Experiment verification  
Carrying capacity

## ABSTRACT

In the field of energy harvesting and self-powered sensing, the universal equivalent circuit model of triboelectric nanogenerators (TENGs) is an important development tool for research and applications. Such a universal model of the current source is established to first order for the basic operating modes of a TENG, which provide the related theoretical models and electrical models used in simulation. The universal first-order equivalent circuit model demonstrates that the carrying capacity of a TENG separates into three regions of distinct output characteristics, namely, constant current, maximum power, and constant voltage. Moreover, employing electrometers, an electrometer and multimeters, and TENGs in series and parallel in successive experiments, we verify that the TENG can be considered a current source with a resistance of mega-ohms and a capacitance of nano-farads. Overall, our first-order model sets electrical standards for the internal circuit of the TENG and therefore provides theoretical guidance that lays the foundation for applications in high-performance supply and grid-connected power generation.

## 1. Introduction

In 2012, Wang's group [1] first proposed the triboelectric nanogenerator (TENG) that converted widely distributed mechanical energy into electrical energy [2–5]. There are four distinct working modes classified by their operation: two normal modes of motion, called contact-separation (C-S) [6,7] and single-electrode (S-E) [8,9], and two tangential modes of motion, called lateral-sliding (L-S) [10,11] and free-standing (F-S) [12,13]. Because TENGs can be made of various materials and display good low-frequency characteristics, they have significant value in research and applications as micro/nano power sources and self-powered sensing, as well as blue energy and high-voltage sources [14–18].

As is known to all, theory and applications of TENGs have progressed with further research [19–23] that has deepened the understanding of their mechanism [24–27]. Indeed, when a TENG uses a bridge rectifier to charge a capacitance, its operation is equivalent to a direct-current voltage source with a constant internal resistance [28,29]. Moreover,

by comparing electromagnetic power generation methods, the TENG can be considered a constant current source with a large internal resistance [30–32]. The research hints at the electrical mechanism of the TENG being important [33–35] and its equivalent circuit model being central in the theoretical assessments of the output performance and engineering applications for grid-connected power generation [36–38]. Therefore, analyzing the internal circuit, evaluating the power source, and establishing a more explicit and universal first-order equivalent circuit model (FO-ECM) of the TENG is essential [39–41].

Hence, a universal FO-ECM of the current source is established by analyzing the working output of the various operating modes of the TENG. This model was verified in simulations of the theoretical model and the electronic circuit. The carrying capacity of the TENG was found to separate into three regions. A detailed experimental verification was conducted from measurements taken in experiments using separately electrometers, an electrometer and multimeters, and TENGs both in series and in parallel. With its verification, the FO-ECM sets electrical standards for the internal circuits of the TENG and provides valuable guidance on reactance matching that is pertinent for theoretical

\* Corresponding authors at: Beijing Institute of Nanoenergy and Nanosystems, Chinese Academy of Sciences, Beijing 101400, China.

E-mail addresses: [zhong.wang@mse.gatech.edu](mailto:zhong.wang@mse.gatech.edu) (Z.L. Wang), [chengtinghai@binn.cas.cn](mailto:chengtinghai@binn.cas.cn) (T. Cheng).

<sup>1</sup> These authors contributed equally to this work.

Nomenclature	
FO-ECM	the first-order equivalent circuit model
C-S mode	contact-separation mode
L-S mode	lateral-sliding mode
S-E mode	single-electrode mode
F-S mode	free-standing mode
CC-OCR	constant current output characteristic region
MP-OCR	maximum power output characteristic region
CV-OCR	constant voltage output characteristic region
$V_A$	voltage measured by electrometer
$V_B$	voltage measured by multimeter
$A_A$	current measured by electrometer
$Z_L$	external branch load impedance
//	parallel connection
+	series connection
AC	alternating current
$I_0$	current in the current source model
$R_0$	internal resistance
$C_0$	internal capacitance
$I_1$	current of the outer branch
$I_{R_0}$	current of internal resistance
$V_{R_0}$	load voltage of $R_0$
$R_L$	load resistance
$V_{R_L}$	load voltage of $R_L$
$Z_R$	equivalent impedance of $R_L$
$f$	frequency of AC
$V_{oc}$	open-circuit voltage
$I_{sc}$	short-circuit current

developments and practical applications of the TENG.

## 2. Theory and simulation analysis

### 2.1. Model establishment

TENGs operate in four basic working modes (Fig. 1 a–d), each of which can be prescribed a FO-ECM (Fig. 1e) based on their electrical characteristics, namely, current  $I_0$ , internal resistance  $R_0$ , and internal variable capacitance  $C_0$ . Here, the resistor is connected in parallel with the current source and in series with the capacitor. The TENG is considered a current source because when measuring the devices in series or in parallel the voltage is divided. The performance of two TENGs in parallel subsequently improves. Conversely, the performance of two TENGs in series remains unchanged [23]. Because there is a layer of non-conductive polymer material between the two electrodes, the TENG has a large internal resistance. Given the basic working principle of the TENG, an internal capacitance develops, and during operations,

the TENG acts as a variable capacitor.

The equivalent circuit model of the TENG is established from Kirchoff's current law at the junctions; that is, the internal current  $I_0$  is the sum of the current of the internal resistor  $I_{R_0}$  and the current  $I_1$  in the outer branch connecting the load,

$$I_0 = I_1 + I_{R_0} \quad (1)$$

Applying Ohm's law, with  $V_{R_0}$  the internal voltage and  $R_0$  the internal resistance, Eq. (1) becomes

$$I_0 = I_1 + \frac{V_{R_0}}{R_0} \quad (2)$$

Given load resistance  $R_L$ , the equivalent impedance  $Z_R$  of the outer branch is

$$Z_R = \sqrt{R_L^2 + \left(\frac{1}{2\pi f C_0}\right)^2} \quad (3)$$

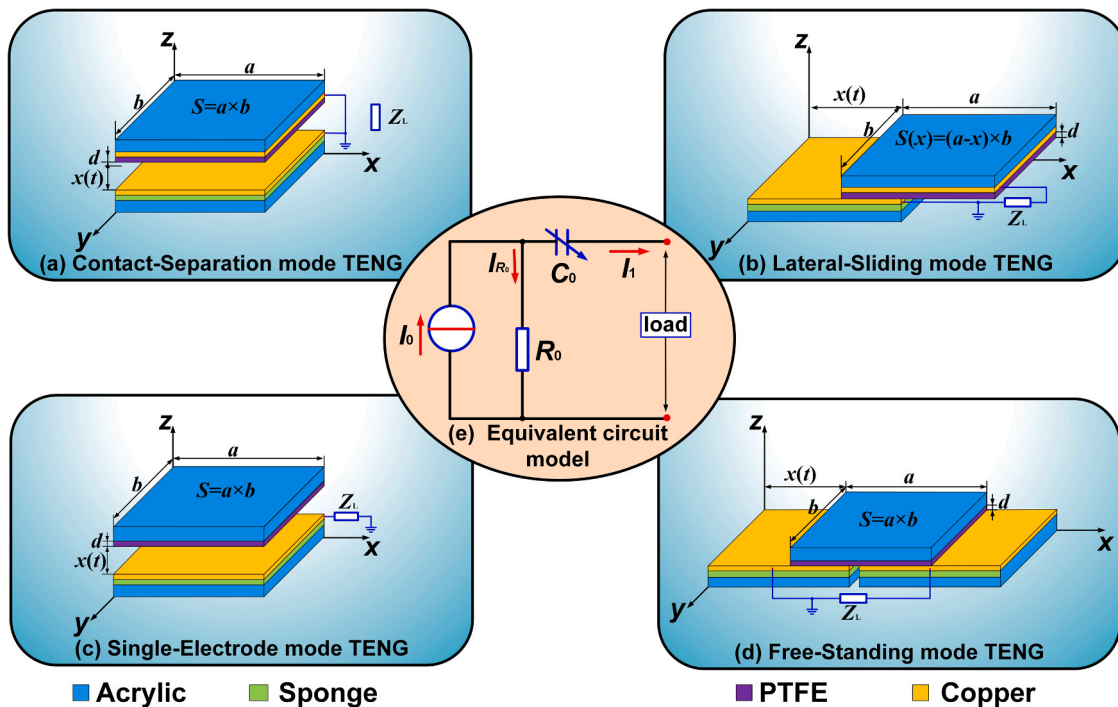


Fig. 1. Theoretical model of the equivalent circuit for a TENG: (a) contact-separation mode (C-S mode), (b) lateral-sliding mode (L-S mode), (c) single-electrode mode (S-E mode), and (d) free-standing mode (F-S mode); (e) equivalent circuit model.

Because the voltages of the two branches are equal, we obtain

$$V_{R_0} = \frac{V_{R_L}}{R_L} \sqrt{R_L^2 + \left(\frac{1}{2\pi f C_0}\right)^2}, \quad (4)$$

where  $V_{R_L}$  denotes the voltage across the load resistor, and  $f$  the frequency of the alternating-current signal passing through the internal capacitor. Combining Eqs. (2) and (4) yields  $I_0$  for the current source model,

$$I_0 = \begin{cases} \frac{V_{R_L}}{R_L} + \frac{V_{R_L}}{R_0} \sqrt{R_L^2 + \left(\frac{1}{2\pi f C_0}\right)^2}, & R_L \neq 0 \\ I_1 + \frac{I_1 \left(\frac{1}{2\pi f C_0}\right)}{R_0}, & R_L = 0 \end{cases} \quad (5)$$

Here, frequency  $f$  can be regarded as the working frequency of TENG. The load voltage  $V_{R_L}$  and load current  $I_1$  can now be determined from Eq. (5) in the forms,

$$V_{R_L} = \frac{I_0 R_0 R_L}{R_0 + \sqrt{R_L^2 + \left(\frac{1}{2\pi f C_0}\right)^2}}, \quad (6)$$

$$I_1 = \frac{I_0 R_0}{R_0 + \sqrt{R_L^2 + \left(\frac{1}{2\pi f C_0}\right)^2}}. \quad (7)$$

These two expressions dictate the open-circuit voltage  $V_{oc}$  and short-circuit current  $I_{sc}$ ,

$$V_{oc, R_L \rightarrow +\infty} = I_0 R_0, \quad (8)$$

$$I_{sc, R_L=0} = \frac{2\pi f C_0 R_0 I_0}{2\pi f C_0 R_0 + 1}. \quad (9)$$

In the theoretical calculations applying our FO-ECM, geometrical expressions for resistance and capacitance are inserted in Eq. (5) to give for the internal current,

$$I_0 = \begin{cases} \frac{V_{R_L}}{R_L} + \frac{V_{R_L} \sqrt{S^2 + \left(\frac{2kd}{f\epsilon_r\epsilon_0 R_L}\right)^2}}{\rho L}, & R_L \neq 0 \\ I_1 + \frac{I_1 \left(\frac{2kd}{f\epsilon_r\epsilon_0}\right)}{\rho L}, & R_L = 0 \end{cases} \quad (10)$$

where the electrical resistance  $R_0$  is related to the cross-sectional area of the resistor  $S$ , length  $L$ , and resistivity  $\rho$ . For parallel plates, the capacitance  $C_0$  is related to the plate area  $S$ , relative distance  $d$ , relative permittivity  $\epsilon_r$ , vacuum permittivity  $\epsilon_0$ , and  $k$  is the constant of electrostatic force.

Similarly, with load capacitance  $C_L$ , Eq. (5) yields

$$I_0 = 2\pi f C_L V_{C_L} + \frac{V_{C_L} \left(S + \frac{4\pi kd}{\epsilon_r \epsilon_0} C_L\right)}{\rho L} \quad (11)$$

where  $V_{C_L}$  denotes the voltage of load capacitor [see Supporting Information Note 1, Eqs. (S1–S8)].

The maximum values of the internal resistance and the internal capacitance for the TENG are constant. The output performance of the TENG is related to parameters such as area, thickness, and dielectric constant that rise in the capacitance and resistance formulae. With the TENG's internal resistance and internal capacitance maintaining values of mega-ohms and nano-farads, respectively, estimates can be derived [see Supporting Information Note 1, Eqs. (S9–S12)].

In brief, the output performance of the TENG is directly related to the load; load voltage is linearly dependent with load resistance, and the load current is inversely dependent with load resistance. Therefore, according to the theoretical model, the load resistance establishes three different regions. When the reactance of the load resistance is greater than the internal capacitance, the load current remains almost constant but is at a low level, whereas the voltage remains almost constant but is at a high level. When the impedance of the load resistor is smaller than internal capacitance and larger than the internal resistance, a change in load resistance induces an obvious change in the current on the load branch. Hence, the rate of change in voltage of the load resistor is faster. When the impedance of the load resistor is smaller than the internal resistance and the resistance changes, the current in the load resistor approaches that of the current source. Therefore, the load resistance becomes linearly proportional to the load voltage. Conversely, a negative correlation develops between load voltage and capacitance, and a positive correlation develops between load current and load capacitance. This trend is opposite to that of load resistance.

## 2.2. Simulation analysis

Circuit simulations of the FO-ECM were performed (Fig. 2a). The simulation software and related parameter settings are listed in Table S1. The voltage and current curves (Fig. 2b) under different load resistances and capacitances show that, with increasing resistance, load voltage rises and load current decreases, whereas, with increasing capacitance, load voltage falls and load current increases. These load curves feature three regions differing in properties regardless of capacitive or resistive loading. In the first region (Fig. 2b(i)), the current is large and relatively constant, and the voltage rises linearly. In the second region, the load voltage rises rapidly, and the load current drops quickly. The voltage and current curves intersect here, at which point the load power for this TENG reaches a peak. In the third region, the voltage of TENG approaches the open-circuit voltage and remains almost constant, while the current decreases slowly. For capacitive loading (Fig. 2b(ii)), the trend for the curves of load voltage and current are opposite to those for resistive loading (Fig. 2b(i)).

## 3. Results and discussion

The experimental measurements for the C-S and L-S modes include measurements using electrometers, an electrometer and multimeters, and TENGs in series and in parallel. For convenience, the C-S and L-S modes were selected for this study. The essential electrometer measurements and the series-parallel measurements of two TENGs were performed for the other modes.

### 3.1. Measurement by electrometers

The voltage and current curves of a TENG in the C-S mode (Fig. 3(a)) and L-S mode (Fig. 3(b)) were recorded under resistive loading (i) and capacitive loading (ii) respectively. The voltage and current load curves separate into three regions, similar to the trends obtained in simulations. We use resistive loading to illustrate the behavior (Fig. 3a(i), b(i)). The three regions are classified using the electrical characteristics of the TENG. The region less than  $10^6 \Omega$  is called the constant-current output characteristic region (CC-OCR) in which current remains constant, and the voltage tends to increase linearly with increasing load resistance. The region  $10^6 \Omega$ – $10^9 \Omega$  is called the maximum-power output characteristic region (MP-OCR). With increasing resistance, the current drops rapidly, whereas the voltage rises quickly. In this region, voltage and current intersect. Being the product of load voltage and current, the output power peaks at the intersection point. The region above  $10^9 \Omega$  is called the constant-voltage output characteristic region (CV-OCR). With increasing resistance, voltage remains constant while current decreases slowly. However, there is a sudden change in resistance at  $10^9 \Omega$  (Fig. 3a

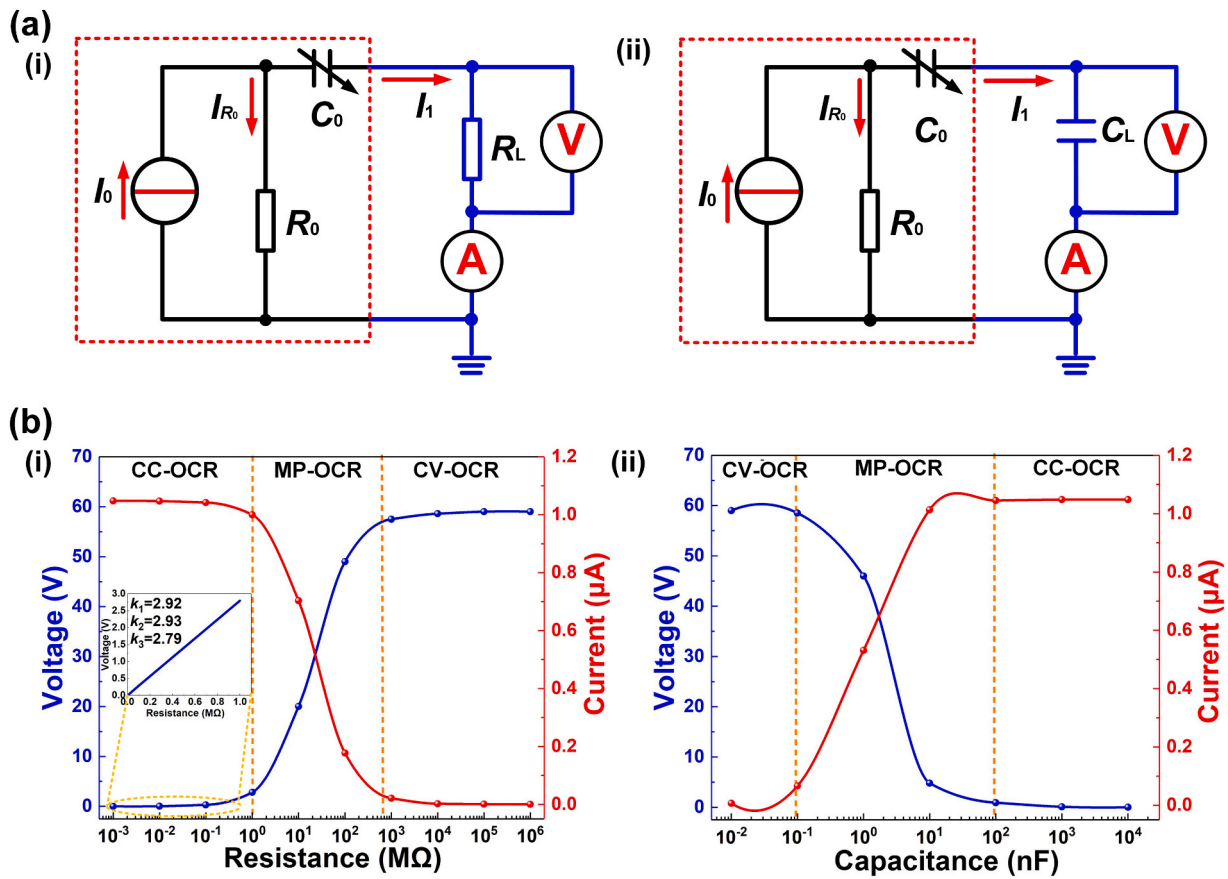


Fig. 2. Simulation circuits (a) and corresponding loading curves (b) under resistive loading (i) and capacitive loading (ii).

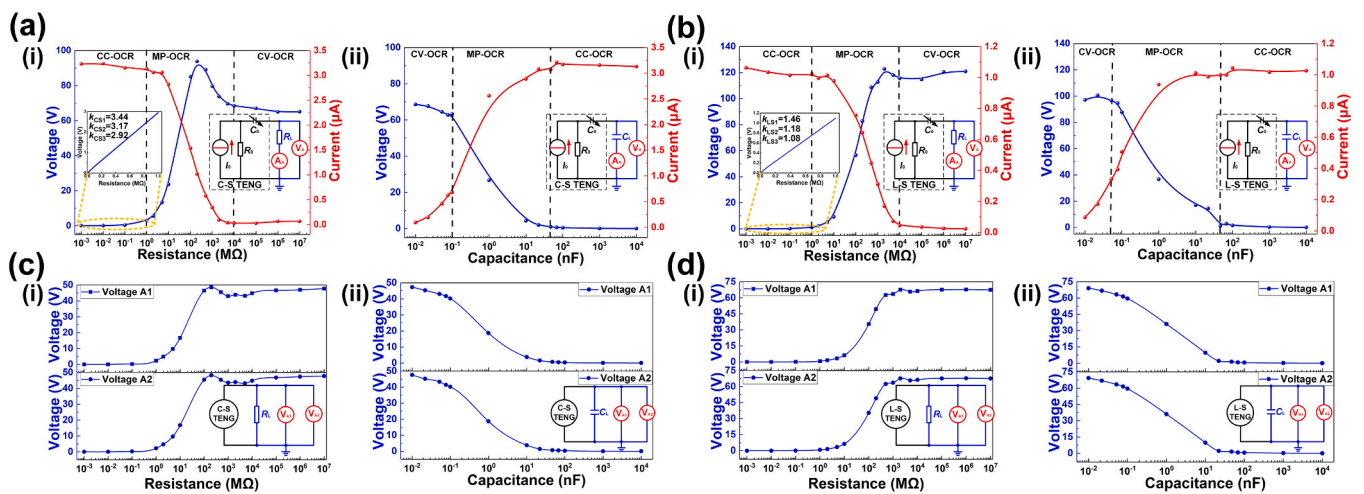


Fig. 3. Voltage and current under different load resistances (i) and capacitances (ii) for contact-separation mode (a, c) and lateral-sliding mode (b, d) obtained from electrometer measurements. (a) and (b) are single electrometer (A) tests. (c) and (d) are from measurements obtained with two electrometers in parallel.

(i). The specific waveform is shown in Fig. S1. The TENG of C-S mode is a discontinuous contact TENG, and its contact time is very short. The charge transfer of TENG is normal when the load is low impedance, and the waveform is comprehensive. However, when the load is high impedance, the charge transfer ability of the TENG decreases, and it can not be completely transferred in its working cycle, thus causing the waveform change of the TENG.

The loading curves of the TENG feature three regions for both resistive and capacitive loading. In this situation, the external resistor is connected in parallel with the internal resistor and in series with the

internal capacitor. When the external resistance is less than the internal resistance  $R_0$ , the CC-OCR ensues. When the load resistance and the internal resistance are at the same level, the MP-OCR occurs. When the reactance of the external resistance is greater than the internal capacitance, voltage and current curves of the CV-OCR arise. Similar results appear for a load capacitor connected in series with the internal capacitor when the reactance of the load capacitor is much smaller than the internal resistance. The smaller the capacitance on this branch, the greater is the voltage, in accordance with the trend for CC-OCR. In the same way, the variation in load capacitance was compared with the

series internal variable capacitance in identifying MP-OCR and CV-OCR. When measuring the performance using two electrometers in sequence, one is grounded in series and hence no data is acquired. Data can only be measured using two electrometers in parallel. The total external load resistance is reduced to half of the original value (Fig. 3c, d). Because the TENG is a current source and the internal resistance of the electrometer is more than 200 TΩ, the performance of the load branch is that of the third region, therefore the total current of the branch is almost unchanged. When the two electrometers are shunted in parallel, the current flowing through each measurement resistor of each electrometer is reduced to half of its original value, so that the voltage measured by each electrometer is half of its original value. (see Supporting video S1). This result confirms the correctness of the FO-ECM and further explains why the TENG has output characteristics of a current source. The measured results for the other modes are consistent with the trends for the C-S and L-S modes (in Fig. S2).

Supplementary material related to this article can be found online at [doi:10.1016/j.nanoen.2021.106335](https://doi.org/10.1016/j.nanoen.2021.106335).

### 3.2. Hybrid measurements using an electrometer and multimeters

Loading curves of the TENG (Fig. 4) were obtained with a multimeter and an electrometer connected in series and in parallel. Fig. 4a shows the test circuits. Fig. 4a(i, ii) show the two measurement devices in series, although when the current is tested by a multimeter and an electrometer in series, the internal equipment is short-circuited. The measurement data is consistent with current data measured using a single electrometer; hence, only an in-series voltage test was conducted. Circuit diagrams with the two devices in parallel are given in Fig. 4a(iii, iv). Fig. 4b and c show the voltage and current curves with the TENG in the C-S and L-S modes. Both the current and voltage curves were measured using an electrometer and multimeter. Voltage values from the electrometer are high for the devices in series but are low for devices in parallel. In addition, when the multimeter and the electrometer are in series (Fig. 4c(i)), voltages measured by the electrometer are high, but when they are in parallel (Fig. 4c(iii)), the voltage values recorded by the electrometer

are low.

The internal resistance of the electrometer is greater than 200 TΩ, and that of the multimeter is 10 MΩ. When the electrometer and the multimeter are connected in series, the load resistance on the test branch is much larger than the internal resistance. Moreover, the TENG can be considered a constant current source because the amount of charge transferred is constant. That is, the measured value is the open-circuit voltage of the TENG, which is related to the internal resistance of the measuring device. Therefore, the electrometer registers a high voltage. When the multimeter is connected in series with the electrometer, the current in the external branch is small and constant. The internal resistance of the multimeter is much smaller than the internal resistance of the electrometer; hence, the voltage registered by the multimeter is smaller (Fig. 4a(i)).

When the electrometer is in parallel with the multimeter and has load  $Z_L$ , the branch current of the multimeter is relatively small and thus the electrometer measures a lower voltage (Fig. 4a(iii)). The voltage displayed by the multimeter depends mainly on the external load. When the electrometer is registering a current, it is in a short-circuit state. This situation is equivalent to the multimeter connected in parallel with load  $Z_L$  (Fig. 4a(iv)).

Various hybrid connections (Fig. 5a), in which an electrometer is connected in parallel with 1–3 multimeters connected in series, were set up and load voltage and current data were recorded. The best output performance was registered by the electrometer with three multimeters in series (Fig. 5(i)). With multiple multimeters in series, the resistance of the branch circuit increases. Therefore, whether the TENG is in the C-S mode (Fig. 5b,c) or L-S mode (Fig. 5d,e), the performance measured by the electrometer is significantly improved. The load resistance increases with the number of multimeters. Moreover, the output performance continues to strengthen, proving that the output characteristics of TENG are the same as the current source (see Supporting video S2 and S3). That is, the hybrid measurements obtained from the electrometer and multimeters verifies the applicability of the FO-ECM.

Supplementary material related to this article can be found online at [doi:10.1016/j.nanoen.2021.106335](https://doi.org/10.1016/j.nanoen.2021.106335).

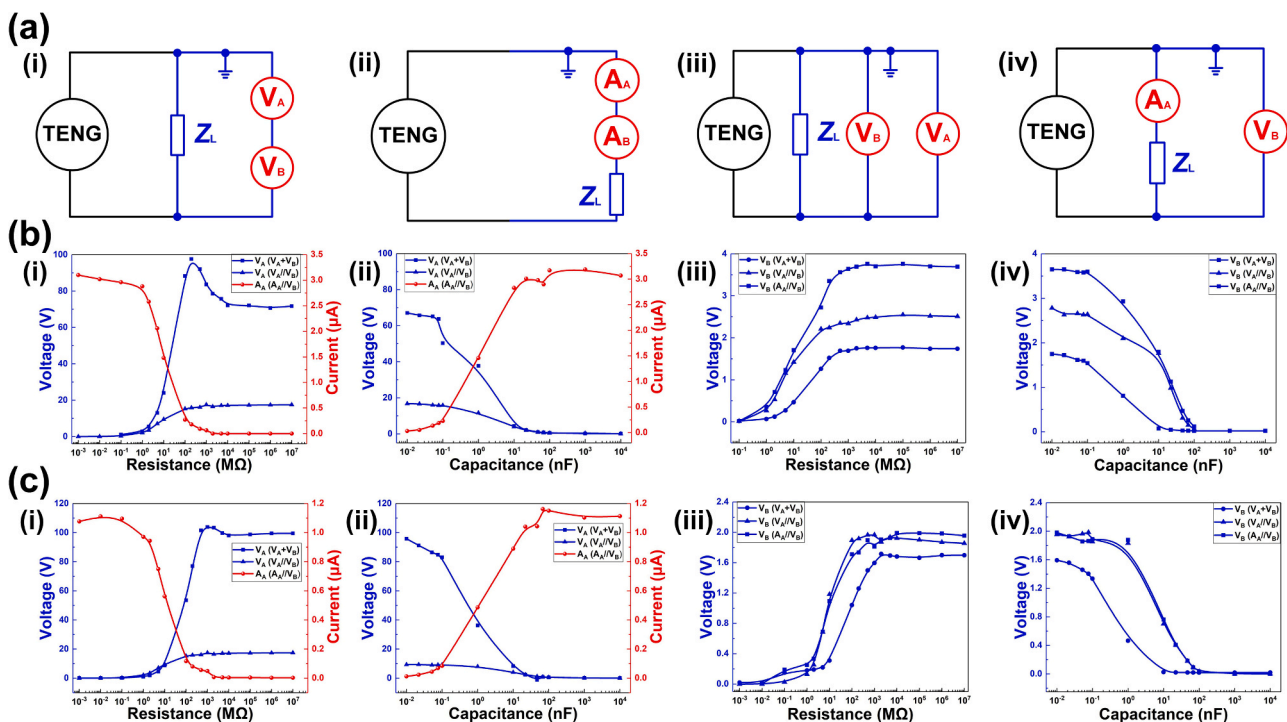


Fig. 4. Voltage and current curves for different load resistances (i, iii) and capacitances (ii, iv) as measured by electrometer (A) and multimeter (B) in series (+) and in parallel (/): (a) test circuits, the TENG in (b) contact-separation and (c) lateral-sliding modes.

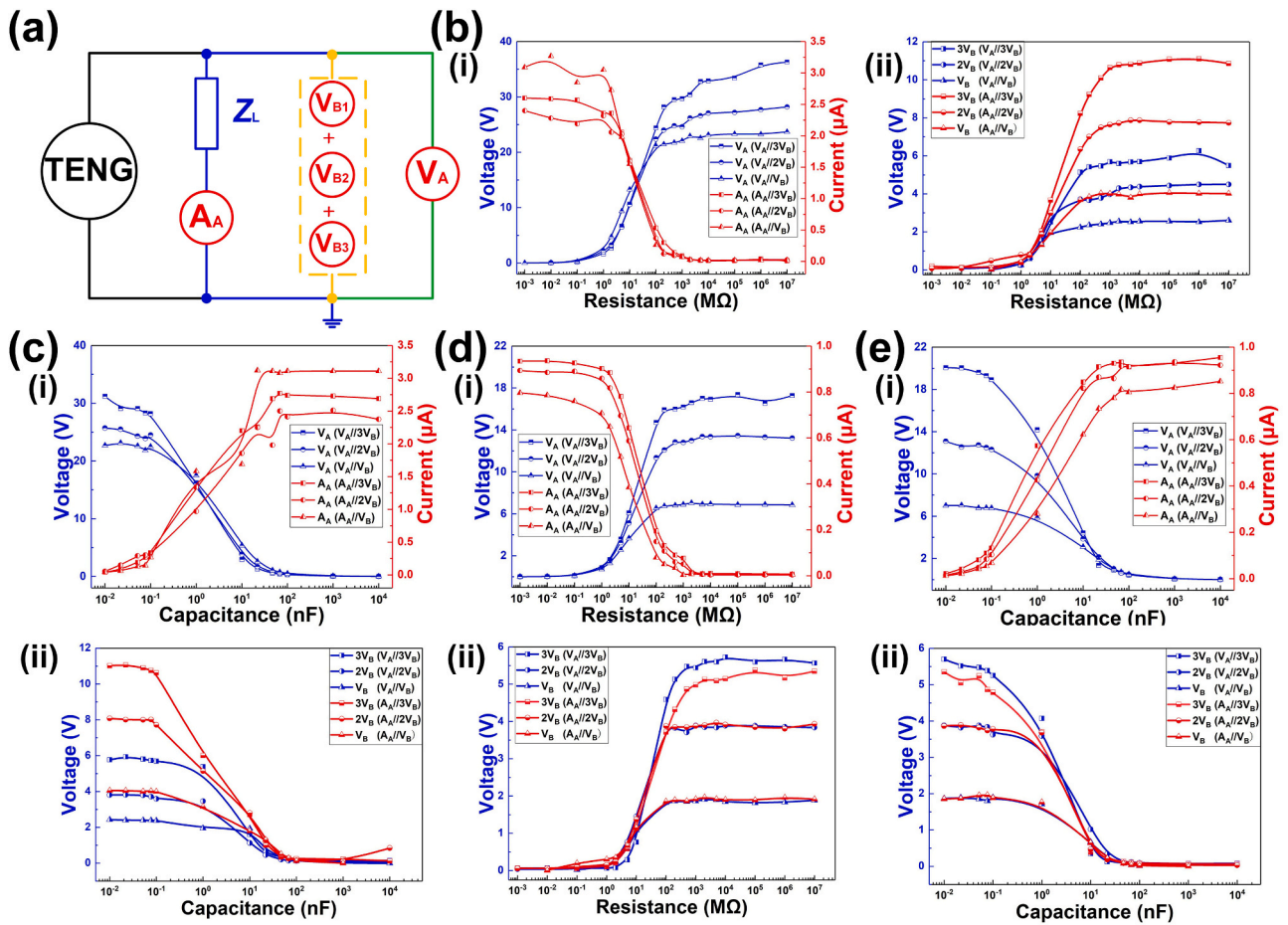


Fig. 5. Voltage and current curves for different load resistances (b, d) and capacitances (c, e) as well as the hybrid connections of measuring device for electrometer (A) and multimeter (B). (a) The test circuit for the TENG operating in (b, c) contact-separation mode and (d, e) lateral-sliding mode.

Supplementary material related to this article can be found online at [doi:10.1016/j.nanoen.2021.106335](https://doi.org/10.1016/j.nanoen.2021.106335).

### 3.3. Measurement of TENGs in series and parallel

The load voltage and current curves were obtained for two TENGs in series and in parallel (Fig. 6a, b) and operating in the C-S and L-S modes,

respectively. The series and parallel connections of TENG1 and TENG2 are shown in Fig. 6a(i, iii) and 6b(i, iii). The basic measurements of TENG1 and TENG2 are shown in Fig. 6a(ii, iv) and b(ii, iv). The test circuit for each TENG setup is illustrated as an inset. The trend in load voltage and current is consistent with previous measurements, which shows that the series/parallel connection of the TENGs conforms to the basic laws of power supply. More importantly, the performance for

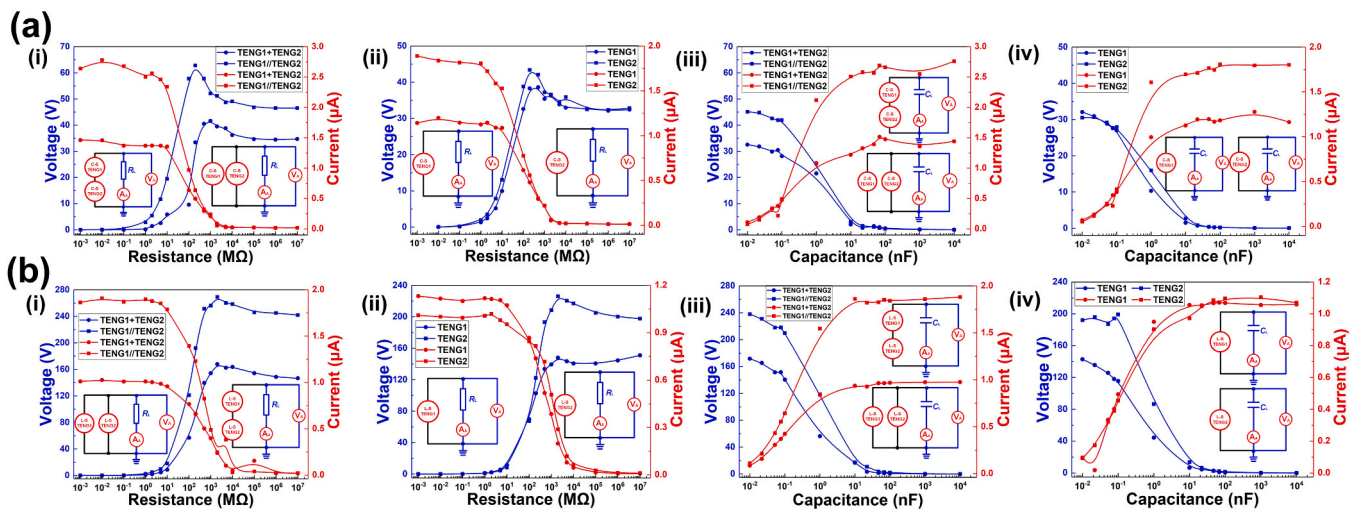


Fig. 6. Voltage and current curves for TENG1 and TENG2 in series (+) and in parallel (/) operating in (a) contact-separation and (b) lateral-sliding modes for different load resistances (i, ii) and load capacitances (iii, iv).

TENG1 and TENG2 are not much different from the basic experimental test. The performance is improved for TENG1 and TENG2 in parallel, and the output performance in series is similar to a single TENG (see Supporting video S4). This fact is attributed to the power supply of the TENG being a current source, and the performance of current sources in parallel increases, whereas the performance for a series setup is equal to that for the maximum current source. In addition, the performance of two TENGs in parallel is not equal to the sum of that of two TENGs. The main reason is that the internal current source of a TENG is not ideal, and with the capacitance varying the TENG resistance is large. Therefore, the performance of the TENG depends on the equivalent circuit model. The trends in the load performance for the other modes are shown in Fig. S3. The load voltage and current for a TENG operating in the S-E and F-S modes are consistent with the C-S and L-S modes, which show that the FO-ECM well describes the four basic operating modes. Moreover, the series/parallel setups for two TENGs demonstrate the reliability of the FO-ECM.

Supplementary material related to this article can be found online at [doi:10.1016/j.nanoen.2021.106335](https://doi.org/10.1016/j.nanoen.2021.106335).

Whether two TENGs are connected either in series or in parallel, the point of intersection of the current and voltage curves appears at mega-ohm levels for different resistive loadings and at nano-farad levels for different capacitive loadings. Therefore, the TENG's internal resistance and capacitance are at megaohm and nano-farad levels, respectively. That is, the TENG acts as a current source with the FO-ECM being a more suitable internal circuit model governing the TENG operating principle.

#### 4. Conclusions

The universal FO-ECM of the current source was established for the TENG. A theoretical model of the TENG with load voltage was derived in accordance with the FO-ECM. The open-circuit voltage and short-circuit current were obtained; these govern the theoretical relationship between the TENG and load resistance. Moreover, the behavior of the FO-ECM of the current source were verified in circuit simulations. Model simulations showed that the carrying capacity features three output characteristic regions: specifically, constant current, maximum power (in which load current and voltage vary significantly and the maximum power point appears), and constant voltage. Finally, this model was verified using measurement data obtained using in separate experiments electrometers, an electrometer and multimeters, and two TENGs both in series and in parallel. The experimental results confirmed that the power supply of the TENG is a current source with mega-ohm-level internal resistance and nano-farad-level internal capacitance. The FO-ECM of the TENG established an internal circuit standard. Moreover, the model offers theoretical guidance in reactance matching, laying the foundation for further practical applications of TENGs.

#### 5. Experimental section

##### 5.1. Fabrication of TENG

The fabrication materials used in TENG of contact-separation (C-S) and lateral-sliding (L-S) modes are polytetrafluoroethylene (PTFE, thickness of 80  $\mu\text{m}$ ) and copper electrodes (thickness of 65  $\mu\text{m}$ ). The electrode form of TENG is shown in Fig. S4. For the single-electrode (S-E) and free-standing (F-S) modes, a single circular TENG is used in the series-parallel experiment of the test device. The diameter of the circle electrode is 50 mm and 70 mm, respectively. When both TENGs are connected in series and parallel, the circular electrode is divided into two semicircular electrodes to ensure the same frequency of the 2 TENGs (Fig. S4a, c). For the L-S and F-S mode, square electrodes are used, and the length and width are  $70 \times 50 \text{ mm}^2$  and  $40 \times 40 \text{ mm}^2$ , respectively. Only a single TENG is used for measurement in the series and parallel experiment of the measurement device. When two TENGs in series or parallel, two TENGs are used for measurement (Fig. S4b, d).

##### 5.2. Measurement environment

During the test, the constant temperature and humidity box (Y-HF-960L, Yuhangzhida, China) are used to control the temperature and humidity. The temperature and relative humidity are maintained at 25  $^{\circ}\text{C}$  and 45%, respectively. A two-phase hybrid servo motor (DE60HB102-1000, Vimidi, China) drives TENG for experiments, and the drive frequency is 1 Hz. The force and distance are shown in Figs. S5 and S6, Supporting Information Note 2. For the C-S mode, the moving distance is controlled at 5 mm, and the force sensor (Model 41, Honeywell, USA) is used for force control, and the force is 13.5 N. For the L-S mode, the moving distance is 50 mm and a 500 g weight is used to pressurize. The force is 9.77 N. In addition, for the L-S mode, the force of TENG can be changed by adding weights.

##### 5.3. Device of measurement

The output signal is collected by an electrometer (6514, Keithley, USA) and a multimeter (UT58A, UNI-T, China). The signal of electrometer collecting is converted by a data acquisition system (USB-6218, National Instruments, USA). The display and storage of data are performed by installing the software LabVIEW with the computer. Moreover, all load voltage and current value points are the peak-to-peak points of the collected waveform in this paper.

#### CRediT authorship contribution statement

**Da Zhao:** Investigation, Writing - original draft, Validation. **Xin Yu:** Conceptualization, Investigation, Writing - original draft, Validation. **Zhenjie Wang:** Investigation, Validation. **Jianlong Wang:** Investigation, Validation. **Xiang Li:** Investigation. **Zhong Lin Wang:** Conceptualization, Resources, Writing - review & editing, Supervision. **Tinghai Cheng:** Conceptualization, Resources, Writing - review & editing, Supervision.

#### Declaration of Competing Interest

The authors declare that they have no known competing financial interests or personal relationships that could have appeared to influence the work reported in this paper.

#### Acknowledgements

The authors are grateful for the supports received from the National Key R&D Project from the Minister of Science and Technology (Nos. 2016YFA0202701 and 2016YFA0202704) and the Beijing Municipal Science and Technology Commission (No. Z171100002017017).

#### Appendix A. Supporting information

Supplementary data associated with this article can be found in the online version at [doi:10.1016/j.nanoen.2021.106335](https://doi.org/10.1016/j.nanoen.2021.106335).

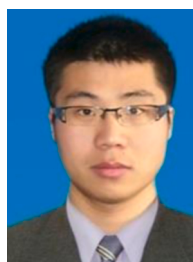
#### References

- [1] F.R. Fan, Z.Q. Tian, Z.L. Wang, Flexible triboelectric generator, *Nano Energy* 1 (2) (2012) 328–334, <https://doi.org/10.1016/j.nanoen.2012.01.004>.
- [2] B. Chen, Y. Yang, Z.L. Wang, Scavenging wind energy by triboelectric nanogenerators, *Adv. Energy Mater.* 8 (10) (2018), 1702649, <https://doi.org/10.1002/aenm.201702649>.
- [3] C. Ye, K. Dong, J. An, J. Yi, Z.L. Wang, A triboelectric–electromagnetic hybrid nanogenerator with broadband working range for wind energy harvesting and a self-powered wind speed sensor, *ACS Energy Lett.* 6 (2021) 1443–1452, <https://doi.org/10.1021/acsenenergylett.1c00244>.
- [4] L. Xu, T. Jiang, P. Lin, J.J. Shao, C. He, W. Zhong, X.Y. Chen, Z.L. Wang, Coupled triboelectric nanogenerator networks for efficient water wave energy harvesting, *ACS Nano* 12 (2) (2018) 1849–1858, <https://doi.org/10.1021/acsnano.7b08674>.
- [5] M. Yin, X.H. Lu, G.D. Qiao, Y.H. Xu, Y.Q. Wang, T.H. Cheng, Z.L. Wang, Mechanical regulation triboelectric nanogenerator with controllable output performance for

- random energy harvesting, *Adv. Energy Mater.* 10 (22) (2020) 8899, <https://doi.org/10.1002/aenm.202000627>.
- [6] L. Cheng, Q. Xu, Y.B. Zheng, X.F. Jia, Yong Qin, A self-improving triboelectric nanogenerator with improved charge density and increased charge accumulation speed, *Nat. Commun.* 9 (2018) 3773, <https://doi.org/10.1038/s41467-018-06045-z>.
- [7] R.D.I.G. Dharmasena, K.D.G.I. Jayawardena, C.A. Mills, J.H.B. Deane, J.V. Anguita, R.A. Dorey, S.R.P. Silva, Triboelectric nanogenerators: providing a fundamental framework, *Energy Environ. Sci.* 10 (2017) 1801–1811, <https://doi.org/10.1039/C7EE01139C>.
- [8] X.Y. Chen, Y.L. Wu, J.J. Shao, T. Jiang, A.F. Yu, L. Xu, Z.L. Wang, On-skin triboelectric nanogenerator and self-powered sensor with ultrathin thickness and high stretchability, *Small* 13 (2017), 1702929, <https://doi.org/10.1002/sml.201702929>.
- [9] F. Zhan, A.C. Wang, L. Xu, S.Q. Lin, J.J. Shao, X.Y. Chen, Z.L. Wang, Electron transfer as a liquid droplet contacting a polymer surface, *ACS Nano* 14 (2020) 17565–17573, <https://doi.org/10.1021/acsnano.0c08332>.
- [10] J.J. Shao, T. Jiang, W. Tang, X.Y. Chen, L. Xu, Z.L. Wang, Structural figure-of-merits of triboelectric nanogenerators at powering loads, *Nano Energy* 51 (2018) 688–697, <https://doi.org/10.1016/j.nanoen.2018.07.032>.
- [11] S.M. Niu, Y. Liu, S.H. Wang, L. Lin, Y.S. Zhou, Y.F. Hu, Z.L. Wang, Theory of sliding-mode triboelectric nanogenerators, *Adv. Mater.* 25 (2013) 6184–6193, <https://doi.org/10.1002/adma.201302808>.
- [12] S.H. Wang, Y.N. Xie, S.M. Niu, L. Lin, Z.L. Wang, Freestanding triboelectric-layer-based nanogenerators for harvesting energy from a moving object or human motion in contact and non-contact modes, *Adv. Mater.* 26 (2014) 2818–2824, <https://doi.org/10.1002/adma.201305303>.
- [13] S.M. Niu, Y. Liu, X.Y. Chen, S.H. Wang, Y.S. Zhou, L. Lin, Y.N. Xie, Z.L. Wang, Theory of freestanding triboelectric-layer-based nanogenerators, *Nano Energy* 12 (2015) 760–774, <https://doi.org/10.1016/j.nanoen.2015.01.013>.
- [14] W.H. Xu, H.X. Zheng, Y. Liu, X.F. Zhou, C. Zhang, Y.X. Song, X. Deng, M. Leung, Z. B. Yang, R.X. Xu, Z.L. Wang, X.C. Zeng, Z.K. Wang, A droplet-based electricity generator with high instantaneous power density, *Nature* 578 (2020) 392–396, <https://doi.org/10.1038/s41586-020-1985-6>.
- [15] C. Zhang, J.K. Chen, W.P. Xuan, S.Y. Huang, B. You, W.J. Li, L.L. Sun, H. Jin, X. Z. Wang, S.R. Dong, J.K. Luo, A.J. Flewitt, Z.L. Wang, Conjunction of triboelectric nanogenerator with induction coils as wireless power sources and self-powered wireless sensors, *Nat. Commun.* 11 (1) (2020) 58, <https://doi.org/10.1038/s41467-019-13653-w>.
- [16] Z.L. Wang, T. Jiang, L. Xu, Toward the blue energy dream by triboelectric nanogenerator networks, *Nano Energy* 39 (2017) 9–23, <https://doi.org/10.1016/j.nanoen.2017.06.035>.
- [17] R. Lei, Y.X. Shi, Y.F. Ding, J.H. Nie, S.Y. Li, F. Wang, H. Zhai, X.Y. Chen, Z.L. Wang, Sustainable high-voltage source based on triboelectric nanogenerator with a charge accumulation strategy, *Energy Environ. Sci.* 13 (2020) 2178–2190, <https://doi.org/10.1039/D0EE01236J>.
- [18] Z.L. Wang, Triboelectric nanogenerator (TEENG)—sparking an energy and sensor revolution, *Adv. Energy Mater.* 10 (17) (2020), 2000137, <https://doi.org/10.1002/aenm.202000137>.
- [19] Z.L. Wang, On the first principle theory of nanogenerators from Maxwell's equations, *Nano Energy* 68 (2020), 104272, <https://doi.org/10.1016/j.nanoen.2019.104272>.
- [20] Y. Liu, S.M. Niu, Z.L. Wang, Theory of tribotronics, *Adv. Electron. Mater.* 1 (9) (2015), 1500124, <https://doi.org/10.1002/aelm.201500124>.
- [21] Z.L. Wang, On Maxwell's displacement current for energy and sensors: the origin of nanogenerators, *Mater. Today* 20 (2) (2017) 74–82, <https://doi.org/10.1016/j.mattod.2016.12.001>.
- [22] S.M. Niu, S.H. Wang, Y. Liu, Y.S. Zhou, L. Lin, Y.F. Hu, K.C. Pradela, Z.L. Wang, A theoretical study of grating structured triboelectric nanogenerators, *Energy Environ. Sci.* 7 (2014) 2339–2349, <https://doi.org/10.1039/C4EE00498A>.
- [23] W.H. Zhang, G.Q. Gu, H.F. Qin, S.M. Li, W.Y. Shang, T.Y. Wang, B. Zhang, P. Cui, J. M. Guo, F. Yang, G. Cheng, Z. Du, Measuring the actual voltage of a triboelectric nanogenerator using the non-grounded method, *Nano Energy* 77 (2020), 105108, <https://doi.org/10.1016/j.nanoen.2020.105108>.
- [24] K. Zhao, G.Q. Gu, Y.N. Zhang, B. Zhang, F. Yang, L. Zhao, M.L. Zheng, G. Cheng, Z. L. Du, The self-powered CO<sub>2</sub> gas sensor based on gas discharge induced by triboelectric nanogenerator, *Nano Energy* 53 (2018) 898–905, <https://doi.org/10.1016/j.nanoen.2018.09.057>.
- [25] M.Y. Xu, T.C. Zhao, C. Wang, S.L. Zhang, Z. Li, X.X. Pan, Z.L. Wang, High power density tower-like triboelectric nanogenerator for harvesting arbitrary directional water wave energy, *ACS Nano* 13 (2) (2019) 1932–1939, <https://doi.org/10.1021/acsnano.8b08274>.
- [26] W.H. Zhang, G.Q. Gu, W.Y. Shang, H.C. Luo, T.Y. Wang, B. Zhang, P. Cui, J.M. Guo, F. Yang, G. Cheng, Z.L. Du, A general charge compensation strategy for calibrating the voltage of a triboelectric nanogenerator measured by a capacitive circuit, *Nano Energy* 86 (2021), 106056, <https://doi.org/10.1016/j.nanoen.2021.106056>.
- [27] H.F. Qin, G.Q. Gu, W.Y. Shang, H.C. Luo, W.H. Zhang, P. Cui, B. Zhang, J.M. Guo, G. Cheng, Z.L. Du, A universal and passive power management circuit with high efficiency for pulsed triboelectric nanogenerator, *Nano Energy* 68 (2020), 104372, <https://doi.org/10.1016/j.nanoen.2019.104372>.
- [28] S.M. Niu, Y.S. Zhou, S.H. Wang, Y. Liu, L. Lin, Y. Bando, Z.L. Wang, Simulation method for optimizing the performance of an integrated triboelectric nanogenerator energy harvesting system, *Nano Energy* 8 (2014) 150–156, <https://doi.org/10.1016/j.nanoen.2014.05.018>.
- [29] S.M. Niu, S.H. Wang, L. Lin, Y. Liu, Y.S. Zhou, Y. Hu, Z.L. Wang, Theoretical study of contact-mode triboelectric nanogenerators as an effective power source, *Energy Environ. Sci.* 6 (2013) 3576–3583, <https://doi.org/10.1039/C3EE42571A>.
- [30] F.R. Fan, W. Tang, Y. Yao, J.J. Luo, C. Zhang, Z.L. Wang, Complementary power output characteristics of electromagnetic generators and triboelectric generators, *Nanotechnology* 25 (2014), 135402, <https://doi.org/10.1088/0957-4484/25/13/135402>.
- [31] N. Zhang, C. Qin, T.X. Feng, J. Li, Z.R. Yang, X.P. Sun, E.J. Liang, Y.C. Mao, X. D. Wang, Non-contact cylindrical rotating triboelectric nanogenerator for harvesting kinetic energy from hydraulics, *Nano Res.* 13 (2020) 1903–1907, <https://doi.org/10.1007/s12274-020-2654-7>.
- [32] X.N. Xia, G.L. Liu, L. Chen, W.L. Li, Y. Xi, H.F. Shi, C.G. Hu, Foldable and portable triboelectric-electromagnetic generator for scavenging motion energy and as a sensitive gas flow sensor for detecting breath personality, *Nanotechnology* 26 (2015), 475402, <https://doi.org/10.1088/0957-4484/26/47/475402>.
- [33] C. Zhang, W. Tang, C.B. Han, F.R. Fan, Z.L. Wang, Theoretical comparison, equivalent transformation, and conjunction operations of electromagnetic induction generator and triboelectric nanogenerator for harvesting mechanical energy, *Adv. Mater.* 26 (22) (2014) 3580–3591, <https://doi.org/10.1002/adma.201400207>.
- [34] Y.F. Gu, T.T. Hou, P. Chen, J.X. Cao, C.X. Pan, W.G. Hu, B.R. Yang, X. Pu, Z. L. Wang, Self-powered electronic paper for scavenging motion energy and information inputs solely from mechanical motions, *Photonics Res.* 8 (9) (2020) 1496–1505, <https://doi.org/10.1364/PRJ.394044>.
- [35] T. Guo, J.Q. Zhao, W.B. Liu, G.X. Liu, Y.K. Pang, T.Z. Bu, F.B. Xi, C. Zhang, X.J. Li, Self-powered hall vehicle sensors based on triboelectric nanogenerators, *Adv. Mater. Technol.* 3 (8) (2018), 1800140, <https://doi.org/10.1002/admt.201800140>.
- [36] Y.K. Pang, Y.T. Cao, M. Derakhshani, Y.H. Fang, Z.L. Wang, C.Y. Cao, Hybrid energy-harvesting systems based on triboelectric nanogenerators, *Matter* 4 (1) (2021) 116–143, <https://doi.org/10.1016/j.matt.2020.10.018>.
- [37] X.D. Yang, L. Xu, P. Lin, W. Zhong, Y. Bai, J.J. Luo, J. Chen, Z.L. Wang, Macroscopic self-assembly network of encapsulated high-performance triboelectric nanogenerators for water wave energy harvesting, *Nano Energy* 60 (2019) 404–412, <https://doi.org/10.1016/j.nanoen.2019.03.054>.
- [38] W.Y. Shang, G.Q. Gu, W.H. Zhang, H.C. Luo, T.Y. Wang, B. Zhang, J.M. Guo, P. Cui, F. Yang, G. Cheng, Z.L. Du, Rotational pulsed triboelectric nanogenerators integrated with synchronously triggered mechanical switches for high efficiency self-powered systems, *Nano Energy* 82 (2021), 105725, <https://doi.org/10.1016/j.nanoen.2020.105725>.
- [39] Z. Wang, W.L. Liu, W.C. He, H.Y. Guo, L. Long, Y. Xi, X. Wang, A.P. Liu, C.G. Hu, Ultrahigh electricity generation from low-frequency mechanical energy by efficient energy management, *Joule* 5 (2) (2021) 441–455, <https://doi.org/10.1016/j.joule.2020.12.023>.
- [40] X. Liang, Z.R. Liu, Y.W. Feng, J.J. Han, L.L. Li, J. An, P.F. Chen, T. Jiang, Z. L. Wang, Spherical triboelectric nanogenerator based on spring-assisted swing structure for effective water wave energy harvesting, *Nano Energy* 83 (2021), 105836, <https://doi.org/10.1016/j.nanoen.2021.105836>.
- [41] M. Wang, J.H. Zhang, Y.J. Tang, J. Li, B.S. Zhang, E.J. Liang, Y.C. Mao, X.D. Wang, Air-flow-driven triboelectric nanogenerators for self-powered real-time respiratory monitoring, *ACS Nano* 12 (2018) 6156–6162, <https://doi.org/10.1021/acsnano.8b02562>.



**Da Zhao** was born in Shandong province, China, in 1994. He received the M.S. degree from Changchun University of Technology, China, in 2020. He is currently studying for his Ph.D. degree in School of Mechatronic Engineering at Changchun University of Technology. He is focused on triboelectric nanogenerators and piezoelectric energy harvester.



**Dr. Xin Yu** is a visiting scholar in Beijing Institute of Nano-energy and Nanosystems, Chinese Academy of Sciences, currently. He obtained the B.S. and Ph.D. degrees from College of Electronic Science and Engineering, Jilin University in 2009 and 2014, respectively. He was a visiting scholar in Department of Electrical and Computer Engineering, Michigan State University from 2017 to 2018. His interests are triboelectric nanogenerators, infrared gas sensing, and photoelectric detection.



**Zhenjie Wang** was born in Hubei Province, China, in 1998. He received a B.E. degree from North China Institute of Science and Technology in Hebei Province, China, in 2019. He is currently studying for a master's degree in the School of Electrical and Electronic Engineering, Changchun University of Technology. His interests are triboelectric nanogenerators, infrared gas sensing, and photoelectric detection.



**Jianlong Wang** was born in 1996 Shandong province, majored in mechanical engineering and received his B.E. degree from Changchun University of Technology. He is currently a master degree candidate under the supervision of Prof. Tinghai Cheng in the same school. His research interest is in the area of triboelectric nanogenerators.



**Xiang Li** was born in 1996 Heilongjiang province, majored in Mechanical Engineering and achieved the B.E. degree from the Shenyang University of Technology in 2018. Now, he is studying for a master's (M.S.) degree in Mechanical Engineering at Shenyang Jianzhu University. His research interest is environmental energy harvesting through triboelectric nanogenerators.



**Prof. Zhong Lin Wang** received his Ph.D. from Arizona State University in physics. He now is the Hightower Chair in Materials Science and Engineering, Regents' Professor, Engineering Distinguished Professor and Director, Center for Nanostructure Characterization, at Georgia Tech. Dr. Wang has made original and innovative contributions to the synthesis, discovery, characterization and understanding of fundamental physical properties of oxide nanobelts and nanowires, as well as applications of nanowires in energy sciences, electronics, optoelectronics and biological science. His discovery and breakthroughs in developing nanogenerators established the principle and technological road map for harvesting mechanical energy from environment and biological systems for powering personal electronics. His research on self-powered nanosystems has inspired the worldwide effort in academia and industry for studying energy for micro-nano-systems, which is now a distinct disciplinary in energy research and future sensor networks. He coined and pioneered the field of piezotronics and piezophotonics by introducing piezoelectric potential gated charge transport process in fabricating new electronic and optoelectronic devices. Details can be found at: <http://www.nanoscience.gatech.edu>.



**Prof. Tinghai Cheng** received the B.S., M.S. and Ph.D. degrees from Harbin Institute of Technology in 2006, 2008 and 2013, respectively. He was a visiting scholar in the School of Materials Science and Engineering at Georgia Institute of Technology from 2017 to 2018. Currently, he is a professor of Beijing Institute of Nanoenergy and Nanosystems, Chinese Academy of Sciences. His research interests are triboelectric nanogenerators, piezoelectric energy harvester, and piezoelectric actuators.